44th AIAA Aerospace Sciences Meeting and Exhibit
9 - 12 January 2006, Reno, Nevada

AIAA 2006-153

Large Eddy Simulation of Soot Formation in Turbulent Premixed Flame

H. El-Asrag[a]*, S. Menon [a]†, T. Lu [b]‡ and C. K. Law [b]§
[a] *School of Aerospace Engineering, Georgia Institute of Technology, Atlanta, 30332.*
[b] *Department of Mechanical and Aerospace Engineering, Princeton University, NJ 08544*

A subgrid model for soot dynamics is developed for large-eddy simulation (LES). The model uses a Method of Moments approach with Lagrangian Interpolative Closure (MOMIC) so that no a priori knowledge of the particles distribution is required. The soot model is implemented within a subgrid mixing and combustion model so that the reaction-diffusion-MOMIC coupling is possible without requiring ad hoc filtering. A relatively detailed multi-species ethylene-air kinetics is employed for the gas phase combustion, and is used here to study the effect of employing a detailed species variable diffusion coefficients on soot production in turbulent premixed flames. The results show that the variable transport properties affect the general structure of the flame in the form of wider curvature probability density function tails and higher turbulent flame speed. In addition, the effect on the relative thermal to molecular diffusivity in the subgrid level (Lewis number effect) changes the surface growth rate and the soot production level.

I. Introduction

Pollution emission control and prediction, is one of the main concerns of most developed industrial countries these days. Soot is mainly a carbonaceous particulate that forms from gas-phase processes due to incomplete combustion of hydrocarbons. Soot has many detrimental effects, for example, the presence of particulate in gas turbine engines can severely affect the lifetime of the blades, and that in turn, will increase the cost of periodic maintenance and life time of the whole engine. The high soot emissivity contributes to the thermal loads of the burner liners and reduces the available heat energy. In addition, soot particulate such as polycyclic aromatic hydrocarbons (PAHs) absorb carcinogenic materials, thereby posing a health hazard for human beings. On the other hand, soot can be useful in industrial furnace applications, when the soot radiation is utilized to increase the load temperature. Hence, the impact of soot on the combustion process and the surrounding environment is important, and needs to be studied carefully.

Measurements[1,2] and modelling[3–5] studies have addressed the physical and dynamical processes of soot formation from the initial gas phase species. Determination of the soot inception, the location in the flame zone where it occurs, and the conditions under which it begins is complicated by the ambiguity in the composition of the soot precursors (PAHs), the species, and the reactions that contribute to the soot formation process.[6] Most measurements are also carried out in laminar or low-turbulence, atmospheric pressure flames. However, in high pressure and in high turbulence regimes (which occur in real combustors) many new issues can become important. For example, turbulent fluctuation in heat transfer and chemical reactions can directly control and/or modify the locations and the processes of the inception, the growth and the oxidation of soot. Increase in the combustor pressure can also impact kinetics and hence, soot formation.

Prediction of soot formation and transport in unsteady turbulent flames is very challenging because both realistic chemical kinetics for gas and soot is required and flow-chemistry interaction over a wide range of spatial and temporal scales has to be resolved. Several steady state approaches have been used to predict soot in realistic configurations. For instance, the laminar flamelet approach combined with a conserved

*Graduate Research Assistant, hossam_el-asrag@ae.gatech.edu
†Professor, AIAA Associate Fellow, suresh.menon@ae.gatech.edu
‡Graduate Research Assistant, tlu@Princeton.edu
§Professor, AIAA Fellow, cklaw@princeton.edu

scalar prescribed PDF[7] and the PDF transport equation.[8] In the past, using a detailed diffusion model was prohibited by the cost of implementation and complexity of the model. Here, an approach for use in large-eddy simulation (LES) is developed and applied to a canonical turbulent premixed-flame interaction problem using a detailed transport model.

II. Formulation of the LES Model

The three-dimensional, multi-species, compressible Navier Stokes equations are solved in the strong conservative form. The fluid is assumed Newtonian with no body forces and in single phase. The LES equations are derived by using spatial Favre filtering[9] and are:[10]

$$\begin{array}{l} \frac{\partial \overline{\rho}}{\partial t} + \frac{\partial \overline{\rho}\widetilde{u_i}}{\partial x_i} = 0 \\ \frac{\partial \overline{\rho}\widetilde{u_i}}{\partial t} + \frac{\partial}{\partial x_j}\Big[\overline{\rho}\widetilde{u_i}\widetilde{u_j} + \overline{p}\delta_{ij} - \overline{\tau_{ij}} + \tau_{ij}^{sgs}\Big] = 0 \\ \frac{\partial \overline{\rho}\widetilde{E}}{\partial t} + \frac{\partial}{\partial x_i}\Big[\Big(\overline{\rho}\widetilde{E} + \overline{p}\Big)\widetilde{u_i} + \overline{q_i} - \widetilde{u_j}\overline{\tau_{ji}} + H_i^{sgs} + \sigma_i^{sgs}\Big] = 0 \end{array} \tag{1}$$

In the above equations, the species conservation equations are not explicitly included, since in the LEM-LES approach they are solved on the subgrid level as will be shown later. In the above equations, $\widetilde{u_i}$ is the i-th filtered velocity component, $\overline{\rho}$ is the filtered density and $\overline{p}$ is the filtered pressure, which is computed from the filtered equation of state: $\overline{p} = \overline{\rho} R_u \sum_{k=1}^{N_s}\left(\frac{\widetilde{Y_k}\widetilde{T}}{W_k} + T_k^{sgs}\right)$. Here, R_u is the universal gas constant, W_k is the k^{th} species molecular weight, N_s is the total number of species, and $\widetilde{Y_k}$ is the filtered k^{th} species mass fraction. The $\widetilde{Y_k}$ in the above relation are obtained from the subgrid closure, as described later.

The filtered total energy per unit mass is defined as $\widetilde{E} = \widetilde{e} + \frac{1}{2}\widetilde{u_k}^2 + k^{sgs}$, where $k^{sgs} = \frac{1}{2}\left[\widetilde{u_k u_k} - \widetilde{u_k}\widetilde{u_k}\right]$ is the subgrid kinetic energy and $\widetilde{e}$ is the filtered internal energy per unit mass given as the sum of the sensible enthalpy and the chemical stored energy as $\widetilde{e} = \sum_{k=1}^{N_s}\widetilde{Y_k h_k} - \overline{p}/\overline{\rho}$. The species enthalpy is calculated from the thermal equation of state: $\widetilde{h_k} = \Delta h_{f,k}^0 + \int_{T_o}^{T} c_{p,k}(\widetilde{T})d\widetilde{T}$, where T_o is the reference standard temperature. Also, $h_{f,k}^0$ is the standard heat of formation at the standard state, $T_o = 298$ K and $P_o = 1$ atm, and $c_{p,k}$ is the specific heat at constant pressure for the k^{th} species. The filtered viscous shear stress ($\overline{\tau_{ij}}$) and heat flux ($\overline{q_i}$) are approximated using the filtered velocity and temperature.[10,11]

The filtered LES equations contain many subgrid terms, denoted by superscript sgs, that require closure. These terms represent the effect of the unresolved motion on the resolved field. The subgrid terms τ_{ij}^{sgs}, H_i^{sgs}, σ_i^{sgs}, and T_k^{sgs} are respectively, the subgrid shear stress, the subgrid heat flux, the subgrid viscous stress, and the subgrid temperature species correlation. These terms are defined as:[10]

$$\begin{array}{l} \tau_{ij}^{sgs} = \overline{\rho}\Big[\widetilde{u_i u_j} - \widetilde{u_i}\widetilde{u_j}\Big] \\ H_i^{sgs} = \overline{\rho}\Big[\widetilde{E u_i} - \widetilde{E}\widetilde{u_i}\Big] + \Big[\overline{p u_i} - \overline{p}\widetilde{u_i}\Big] \\ \sigma_i^{sgs} = \widetilde{u_j \tau_{ji}} - \widetilde{u_j}\overline{\tau_{ji}} \\ T_k^{sgs} = \Big[\widetilde{Y_k T} - \widetilde{Y_k}\widetilde{T}\Big]/W_k \end{array} \tag{2}$$

A. Closure for the LES equations

The closure for the subgrid stresses and subgrid heat flux is achieved using an eddy viscosity model. Such a closure is acceptable since the small-scales primarily provide dissipation for the energy transferred from the large scales. The subgrid model used here is based on the solution of a transport equation for the subgrid kinetic energy, k^{sgs} that has been used extensively for both non-reacting and reacting flows.[11–16]

The k^{sgs} transport equation model is given by:

$$\frac{\partial \overline{\rho} k^{sgs}}{\partial t} + \frac{\partial}{\partial x_i}\Big(\overline{\rho}\widetilde{u_i}k^{sgs}\Big) = -\tau_{ij}^{sgs}\frac{\partial \widetilde{u_i}}{\partial x_j} - C_\epsilon \overline{\rho}\frac{(k^{sgs})^{3/2}}{\overline{\Delta}} + \frac{\partial}{\partial x_i}\Big(\frac{\overline{\rho}\nu_T}{Pr_T}\frac{\partial k^{sgs}}{\partial x_i}\Big) \tag{3}$$

Here, Pr_T is a subgrid Prandtl number, assumed to be unity

The subgrid shear stress and the subgrid heat flux using the k^{sgs} model are, respectively

$$\tau_{ij}^{sgs} = -2\overline{\rho}\nu_T\Big(\widetilde{S_{ij}} - \frac{1}{3}\widetilde{S_{kk}}\delta_{ij}\Big) + \frac{2}{3}\overline{\rho}k^{sgs}\delta_{ij} \tag{4}$$

and

$$H_i^{sgs} = -\frac{\nu_T}{\mathrm{Pr}_T}\frac{\partial \widetilde{H}}{\partial x_i} \tag{5}$$

where the subgrid eddy viscosity is $\nu_T = C_\nu (k^{sgs})^{1/2}\overline{\Delta}$, $\overline{\Delta}$ is the grid filter width and $\widetilde{S_{ij}}$ is the filtered strain rate defined as $\frac{1}{2}\left(\frac{\partial \widetilde{u_i}}{\partial x_j} + \frac{\partial \widetilde{u_j}}{\partial x_i}\right)$. Also, $\widetilde{H} = \widetilde{h} + \widetilde{u_i}\widetilde{u_i}/2 + k^{sgs}$ is the filtered total enthalpy, and $\widetilde{h} = \sum_{k=1}^{N_s} \widetilde{h_k}\widetilde{Y_k}$ is the filtered specific enthalpy. The subgrid viscous work ${\sigma_i}^{sgs}$ and the subgrid temperature-species correlation T_k^{sgs}, are neglected here based on past studies.[11,17] The two model coefficients C_ν and C_ϵ are obtained using a localized dynamic approach as part of the solution.[10]

Since, molecular diffusion, chemical reactions and soot formation occur at the small scales, we extend a subgrid mixing and combustion model developed earlier to non-sooting turbulent flames to study sooting flames. This approach, identified as LEMLES hereafter, has proven quite versatile to simulate turbulent premixed combustion,[18,19] scalar mixing,[12,20,21] non-premixed combustion[12,22] and spray combustion[23,24] without needing any model adjustments. Therefore, we explore its ability to account for soot processes in this study.

B. Chemical Kinetics

For realistic predictions of soot physics, a relatively detailed mechanism is essential (here, we study ethylene-air flames). In addition, it is necessary to define what gas specie is indicative of soot precursor. Although PAHs, benzene and acetylene all have been proposed, we consider acetylene as the key gas species for soot inception. This choice is motivated in part by past observations in ethylene-air premixed flames[25] that acetylene is the main precursor that determines the mass of the soot formed in the inception stage. Another study[26] concluded that most of the soot particle mass comes from C_2H_2 through two main possible paths: the direct addition of acetylene to the soot growing particle and by the addition of acetylene to PAHs, which eventually becomes the soot nuclei.

Therefore, in the present effort we combine an acetylene based four-step soot model[27] that describes nucleation, surface growth, and oxidation with a reduced, but multi-step ethylene-air kinetics model. The kinetics mechanisms for ethylene-air employed here is a semi global 15-step, 19 species mechanism.[28,29]

The detailed mechanism for ethylene oxidation by Qin et al.[30] is the starting mechanism for both the reduced mechanisms. The reduction is guided by densely sampled reaction states, spanning the present parameter range of study, from perfectly stirred reactors (PSR) and auto-ignition, which are respectively representative applications of high- to intermediate-, and low- to intermediate-temperature chemistries. By applying the theory of directed relation graph,[28] 26 important participating species, namely H_2, H, O, O_2, OH, H_2O, HO_2, H_2O_2, C, CH, CH_2, CH_2*, CH_3, CH_4, CO, CO_2, HCO, CH_2O, CH_3O, C_2H_2, C_2H_3, C_2H_4, C_2H_5, $HCCO$, CH_2CO, CH_2CHO, were identified. Two additional species, C_2H_6 and C_3H_6, were retained in the skeletal mechanism in order to lower the reduction error in flame speeds under fuel rich conditions. The final skeletal mechanism therefore consists of 28 species and 167 reactions. By further using computational singular perturbation,[31] ten species, C, CH, CH_2, CH_2*, HCO, CH_3O, C_2H_3, C_2H_5, $HCCO$, and CH_2CHO, were found to be in quasi steady state.

For the current studies, the mechanism is employed in a thermally perfect model in two separate case studies. The first case is with diffusion coefficients determined by using species dependent constant Schmidt number. The second case study is simulated with proper binary variable diffusion coefficients. It was found that the diffusion coefficient of O can be approximated by that of OH; HO_2, H_2O_2, CH_3, and CH_4 by O_2; CO by N_2; CH_2O by CH_2CO; C_2H_2 and C_2H_6 by C_2H_4; and C_3H_6 by CO_2. Thus, by grouping the species with similar diffusion coefficients, only a 9x9 binary diffusion coefficient matrix needs to be calculated in the evaluation of mixture average diffusion coefficients for all the species, resulting in approximately an 80% reduction in CPU time (when compared to the full evaluation). It is noted that in comparison to the previous 16-step mechanism,[28] the current mechanism is not only less by one species but also the number of elementary reactions involved is reduced by about 20%, which is approximately the fraction of CPU time saved in the evaluation of the chemical reaction source terms.

The four-step soot model is:[27,32,33]

$$C_2H_2 \rightarrow^n 2C + H_2 \tag{6}$$

$$C_2H_2 \rightarrow^g 2C + H_2 \tag{7}$$

$$C + \frac{1}{2}O_2 \rightarrow CO \tag{8}$$

$$C + OH \rightarrow CO + H \tag{9}$$

Equation (6) states that the soot monomer is composed of two carbon atoms. Therefore, as long as two carbon atoms come together a soot nuclei is formed. Equation (7) states that the soot reactivity is proportional to the local surface particle area per unit volume and first order in acetylene concentrations. The oxidation of the soot particles by the OH and O_2 species is prescribed by Eqs. (8) and (9).[32,33]

C. Subgrid Model for Soot Formation

To account for soot dynamics in the subgrid model, the Method of Moment (MOM) using Interpolative Closure (MOMIC)[34] is utilized. MOM is based on the idea that the knowledge of all the moments is equivalent to knowing the distribution function itself. MOMIC has the advantage of not requiring a priori knowledge for the particle size distribution function (PSDF). Hence, it is generally applicable, and primarily requires solving a limited (e.g., first few moments) set of differential equations for the time evolution of PSDF moments,[35] which makes this approach cost effective.

Here, we implement the MOMIC approach within the subgrid mixing and combustion model. Details of the original LEMLES is given elsewhere but we repeat here some of the salient features with specific focus on the new features.

In the LEMLES, the gas phase species conservation equations are not spatially filtered as the other LES equations. Rather, the exact unfiltered equations are solved using a two-step Eulerian-Lagrangian approach, and then the resulting scalar fields are ensembled averaged in each LES cell to recover the LES-resolved species mass fractions, $\widetilde{Y_k}$ that is needed in the LES-resolved energy and state equations. The two-step approach can be described by decomposing the total velocity field into the LES-resolved velocity, $\widetilde{u}_i$, the LES-resolved subgrid fluctuations $\left(u_i^{'}\right)^R$ and the unresolved subgrid fluctuations, $\left(u_i^{'}\right)^S$. Thus, a general decomposition of the velocity field can be written as $u_i = \widetilde{u}_i + \left(u_i^{'}\right)^R + \left(u_i^{'}\right)^S$. Using this relation, the unfiltered k^{th} species equation can be written as:

$$\rho\frac{\partial Y_k}{\partial t} + \rho\left[\widetilde{u}_i + \left(u_i^{'}\right)^R + \left(u_i^{'}\right)^S\right]\frac{\partial Y_k}{\partial x_i} - \frac{\partial}{\partial x_i}\left[\rho D_k\frac{\partial Y_k}{\partial x_i}\right] = \dot{\omega_k} \tag{10}$$

Equation (10) is split and solved in a two-step procedure:

$$\frac{Y_k^* - Y_k^n}{\Delta_{t_{LES}}} = -\left[\widetilde{u}_i + \left(u_i^{'}\right)^R\right]\frac{\partial Y_k^n}{\partial x_i} \tag{11}$$

$$\left(Y_k^{n+1} - Y_k^*\right) = \int_t^{t+\Delta_{LES}} -\frac{1}{\rho}\left[\left[\rho\left(u_i^{'}\right)\right]^S\frac{\partial Y_k^n}{\partial x_i} - \frac{\partial}{\partial x_i}\left[\rho D_{i,k}\frac{\partial Y_k^n}{\partial x_i}\right] - \dot{\omega_k^n}\right]dt^{'} \tag{12}$$

Here, the superscript n indicates the LES time level, Δt_{LES} is the LES time-step, D_k is the k^{th} species diffusion coefficient, and $\dot{\omega_k}$ is the k^{th} species production or destruction rate. Equation (11) represents the 3D advection of the scalar field modelled by a Lagrangian transport of the subgrid mass across the LES cells[12] and the integrand in Eq. (12) represents the LEM model that is solved locally inside each LES cell.

In the subgrid implementation of Eq. (12), the species equation (along with a similar equation for the subgrid temperature and soot-related equations) are solved on a 1D domain that is aligned in the direction of the maximum scalar gradient.[36] Thus, the subgrid model takes the following form in the present study:

$$\rho\frac{\partial Y_k}{\partial t^s} = F_k + \frac{\partial}{\partial s}\left[D_k\frac{\partial Y_k}{\partial s}\right] + \dot{\omega_k} \qquad k = 1, \ldots N_s + 1 \tag{13}$$

$$\frac{\partial T}{\partial t^s} = -\frac{1}{\overline{C_p}}\sum_{k=1}^{N_s} C_{p,k}Y_kV_k\frac{\partial T}{\partial s} + \frac{1}{\rho\overline{C_p}}\frac{\partial}{\partial s}\left(\overline{\kappa}\frac{\partial T}{\partial s}\right) - \frac{1}{\rho\overline{C_p}}\sum_{k=1}^{N_s} h_k\dot{\omega_k}W_k + F_T \tag{14}$$

$$\frac{\partial M_r}{\partial t^s} = R_r + C_r + S_r + F_{M_r} \tag{15}$$

The 1D line resolution is chosen to resolve all the turbulent scales below $\overline{\Delta}$ (e.g., the Kolomogrov length scale, η). Here, F_k, F_T and F_{M_r} represent respectively $-\left[\rho\left(u_i^{'}\right)\right]^S \frac{\partial Y_k^n}{\partial x_i}$, the subgrid stirring effect on the species (including soot), and a similar term in the temperature and the moment fields. The stirring process is modelled by stochastic rearrangement process[36] that represents the action of a turbulent eddy (below $\overline{\Delta}$) on the scalar field. In the current implementation, F_{M_r} effect is neglected, but will be revisited in the future.

In Eq. (15), $M_r = \sum_{i=1}^{\infty} m_i^r N_{s_i}$ is the r^{th} moment of the soot particle distribution, defined by the mass m_i and number density N_{s_i} of the soot particles of class size i. The terms R_r, C_r and S_r are respectively, nucleation, coagulation and surface growth effects on the $r-$moment equation. Here, $zero^{th}$ moment M_0 represents the soot number density N_s defined by the number of soot particles per unit volume of the mixture. The first moment M_1 represents the average total mass of soot particles m_s per unit volume. Thus, the soot mass fraction is $Y_s = M_1/\rho$, and the soot volume fraction is $f_v = (\rho Y_s)/\rho_{soot}$, where $\rho_{soot} = 1.8g/cm^3$ is the soot density. Finally, the average particle diameter $d_p = \left(6.0M_2/\pi\rho_{soot}M_1\right)^{1/3}$.

The nucleation effect is modelled here as $R_r = \kappa M_r k_n/\rho_{soot}$, where κ is a calibration constant taken as unity at present, but may need to be adjusted, and k_n is the rate constant of nucleation computed as: $k_n = 0.63x10^4 exp\left(-\frac{21000.0}{T}\right)[C_2H_2]$. This model assumes that the nucleation effect is controlled by the nucleation rate of the carbon atoms by acetylene and that the mass moments grow linearly as nucleation add more particles to the mixture. The surface growth term is computed as:[34]

$$S_r = \pi\left(\frac{6}{\pi\rho}\right)^{2/3}\frac{k_s - k_{ox}}{\Delta m}M_0\sum_{k=0}^{r-1}\Delta m^{r-k}\mu_{r+2/3}, r = 1, 2, 3, \cdots \tag{16}$$

Here, Δm is the mass increment from one size bin to another due to the deposition or abstraction of species from the soot particle surface. If a particle of size m_i gains Δm it will be transferred to the mass bin $i+1$, $\mu_r = M_r/M_o$ is the r^{th} size moment. The rate constants for surface growth and oxidation, k_s and k_{ox} are obtained from:[27,32,33,37]

$$k_s = 0.75x10^3 exp\left(-\frac{12100.0}{T}\right)As_i[C_2H_2] \tag{17}$$

$$k_{ox} = 7.15x10^2\sqrt{T}exp\left(-\frac{19800}{T}\right)As_i[O_2] + 0.36\sqrt{T}As_i[OH] \tag{18}$$

Here, $As_i = \pi d_p^2 M_0$ is the average surface area of the particle of size i per unit mixture volume. Finally, the rate of coagulation (derived from the Smoluchowski equation[38]), is given as:[34]

$$\frac{dC_o}{dt} = -\frac{1}{2}\left(\sum_{i=1}^{\infty}\sum_{j=1}^{\infty}m_i^k\beta_{ij}Ns_iNs_j\right) \tag{19}$$

$$\frac{dC_r}{dt} = \frac{1}{2}\sum_{k=1}^{r-1}\begin{pmatrix} r \\ k \end{pmatrix}\left(\sum_{i=1}^{\infty}\sum_{j=1}^{\infty}m_i^k m_j^{r-k}\beta_{ij}Ns_iNs_j\right) r = 2, 3, ... \tag{20}$$

Here β_{ij} is the collision coefficient between soot particles of class size i and j. According to the flow conditions and the Knudsen number $Kn = \frac{2\lambda}{d_p}$ the molecular regimes is specified and β_{ij} is calculated. The mean free path λ is defined by $\lambda = \left(\sqrt{2}\pi\sigma_g^2 N_s\right)^{-1}$, here, σ_g is the collision diameter of the fluid molecules, and N_s is the number density.[39]

For the continuum regime β_{ij} for coalescent collisions of spherical particles is given by:[40]

$$\beta_{ij}^c = K_c\left(\frac{C_i}{m_i^{\frac{1}{3}}} + \frac{C_j}{m_j^{\frac{1}{3}}}\right)\left(m_i^{\frac{1}{3}} + m_j^{\frac{1}{3}}\right) \tag{21}$$

K_c is given by[41] as $K_c = \frac{2k_BT}{3\nu}$ Where ν is the gas viscosity, and C is the Cunningham slip correction factor and can be expressed as $C = 1 + 1.257Kn$.[35] For the free molecular regime the collision coefficient is calculated from.[40]

$$\beta_{ij}^{f} = K_f \sqrt{\left(\frac{1}{m_i} + \frac{1}{m_j}\right)} \left(m_i^{\frac{1}{3}} + m_j^{\frac{1}{3}}\right)^2 \tag{22}$$

And K_f is given by $K_f = \epsilon \sqrt{\frac{6k_B T}{\rho}} \left(\frac{3}{4\pi\rho}\right)^{\frac{1}{6}}$, where ϵ is the Van Der Waals enhancement factor. Stephen et al.[42] performed a study on the effect of ϵ at different pressures. They showed that this factor ranges from 1.333 and 2.0. Finally, in the transition regime, the collision frequency is usually expressed as the harmonic mean:[43]

$$C_r = \frac{C_r^f C_r^c}{C_r^f + C_r^c} \tag{23}$$

III. Numerical Considerations

Two separate case studies are employed in the current paper for the F1 flame in the thin reaction zone regime. The first case is with diffusion coefficients calculated from a constant species Schmidt number. The other case study is with detailed variable binary diffusion coefficients. Since, the critical C/O ratio for soot formation in ethylene/air premixed flames is around 0.6,[44] we fixed the C/O ratio to 0.677 for all the case studies. The flame test conditions for these cases are summarized in Table 1. The laminar flame properties are extracted from[45] and[46] for initial temperature 307^o k.

Flame	C/O	Re	Da	Ka	$S_L(m/sec)$	$\delta_F(mm)$	$u^{'}$	l(mm)	$\frac{u^{'}}{S_L}$	$\frac{l}{\delta_F}$	$\eta(mm)$
F1	0.67	271	1.152	23.76	0.24	0.108	2.86	1.474	11.90	13.71	0.022

Table 1. Simulated turbulent flame.

The grid resolution is 64x64x64 cube of a physical domain of 1.5x1.5x1.5 mm with 12 LEM cells. The LEM resolution is chosen to capture the flame thickness and to resolve close to the Kolomogrov length scale (1-2 η).[19] Characteristic inflow-outflow conditions are used in the axial direction, and periodic conditions in the transverse and spanwise directions. Inflow turbulence that is superimposed on the mean inflow velocity is assumed to satisfy the von Karman-Pao energy spectrum for isotropic turbulence.[47]

The current approach requires solution of 20 species equations in every LEM domain in every LES cell. Thus, the evaluation of the kinetics is the limiting cost of these simulations. To enhance the computational efficiency, efficient parallel implementation is carried out and in addition, in situ adaptive tabulation (ISAT)[48] is employed in every LES cell to reduce the cost of the chemistry evaluation. The simulation was performed on a dual Intel Xeon (3.4 GHZ) PC cluster. A turn over time for the F1 flame defined as $t_{flow} = l/u^{'}$, takes around 1280 single-processor hours. The results reported here are averaged over 8 turnover times.

IV. Results and Discussion

A. Validation of the Reduced Mechanism

The reduced mechanisms were first validated for homogeneous applications of PSR and auto-ignition, and for diffusive applications of premixed and non-premixed flames. Figures 1 and 2 respectively, compare the reduced mechanism against a detailed one, for ignition delay as a function of initial temperature for stoichiometric C_2H_4/air mixtures, and the deficit temperature, from the corresponding adiabatic flame temperature, as a function of residence time in PSR. It is seen that the reduced mechanism mimics well the performance of the detailed mechanism, with the regimes of largest deviation being of minimal significance. To validate the species concentrations particularly that of C_2H_2, the mass fraction profiles for the important species in a non-premixed counterflow flame are shown in Fig. 3. The agreement can again be considered to be very good. The worst-case error for C_2H_2, approximately 30% on the fuel side, is induced by the elimination of most of the C_3 and C_4 species, which serve as a sink for C_2H_2 leading to even larger molecules involved in soot formation. Considering the uncertainty in the present soot model, the reduction error in

C_2H_2 can be considered to be acceptable, particularly in view of the gain in the computational capability in the simulation.

B. Effect of binary diffusion

Figure 4 shows an instantaneous flame iso-surface for T = 1600 K colored by the density variation, and the axial vorticity magnitude contour at the inflow and outflow plane. The combustion effect is to laminarize turbulence and to reduce the scale magnitude range. The high temperature increases the viscosity, and hence, reduces the Reynolds number. The reduction of the density by heat release reduces the vorticity magnitude by decreasing the misalignment of the pressure, density and velocity vector of rotation. As a result, the heat release effect dissipates the smaller eddies leaving only larger structures behind the flame. The qualitative features of this flow structures and the flame surface are quite similar to the non-sooting cases studied in the past using LEMLES.[19] In the following, we focus primarily on the soot and flame related properties obtained by statistical averaging of the simulated cases.

Ethylene and air nearly have the same molecular weight, hence both molecules diffuse equally in the mixture. Recent studies for laminar flame indicate that ethylene/air mixture has a neutral behavior, since the thermal and molecular diffusivity neutralize each other for a unity Lewis number.[49,50] However, in the turbulence case the flame is highly strained and the curvature effect changes the scalars profiles according to the ratio of the thermal to the molecular diffusivity. The flame stretch is induced by the flow nonuniformity (strain effect) and the curvature due to the wrinkling of the flame surface area, which increases its reaction front. When the flame has negative curvature (concave towards the reactants), the mass is focused towards the products side and the heat is focused inwards to the reactants side. If the Lewis number (Le) is greater than unity, the thermal diffusivity will increase the temperature in the preheat zone and the flame burns strongly with a higher flame temperature.[49] These observations are confirmed in Fig. 5, where the C_2H_4 reaction rate and temperature profile across a concave and a convex flame elements are plotted. The flame shows higher temperature and reaction rate across the concave element.

The fact that the thermal diffusivity focusing effect overcomes the molecular diffusivity defocusing effect indicates that Le > 1. Since, the definition of the indicative Lewis number is not clear, we plotted the mean mixture Lewis number across the flame combined with the mean temperature profile for both cases studied in Fig. 6. Both test cases predict a Lewis number bigger than unity, which coincide with the previous observations. However, the constant Schmidt number case predicts a higher Lewis number, and hence higher thermal diffusivity effect. The closer to unity Lewis number in the variable diffusion case agrees with the literature observations.[49]

Figure 7 shows the pdf of mean curvature for both test cases. The curvature tensor is computed from the following formula:[21]

$$h_{ij} = -\frac{\partial c^2}{\partial x_i \partial x_j}\frac{1}{g} + \frac{1}{g^3}\sum_{k=1}^{3}\frac{\partial c}{\partial x_i}\frac{\partial c}{\partial x_k}\frac{\partial c^2}{\partial x_j \partial x_k} \tag{24}$$

Where $g = \nabla c$, and c is the progress variable taken as 0.8 here. The flame surface curvature is computed as the mean of the two principle radii of curvature computed from the eigenvalues of Eq. (24). The figure shows that the constant diffusion flame is skewed towards the positive curvature (convex towards reactants), while the variable diffusion case is more symmetric with higher probabilities in the negative curvature side. The wide range of curvature indicates the high turbulence effect on the flame structure and the surface area. In addition, the variable diffusivity case shows wider tails and no sharp peaks in the middle. The wider tails indicates the presence of more flames close to the spherical and saddle shapes. The mean in both cases is around zero. These observations are consistent with the past work in non-sooting premixed flames.[51,52]

For Le > 1 the burning rate increases for concave (negative curvature) surfaces due to the concentration of heat in the preheat zone, which consequently lead to a higher burning rates and higher turbulent flame speed (integration of the burning rate). A comparison of the PDF of the mean turbulent flame speed dimensionalized by the laminar unstrained flame speed $\frac{S_T}{S_L} = (1+\beta\frac{u'^{\alpha}}{S_L^{\alpha}})^{1/\alpha}$ is shown in Fig. 8. Where $\alpha = 2$ and β is the minimum of 0.8165 $\frac{u'}{S_L}$ and 16.56.[53] The mean value is around 12 for the variable diffusivity , while the constant Schmidt number case is around 10, with less skewness towards the higher values. This observation is consistent with the curvature PDF shown in Fig. 7.

Finally the effect on the soot formation is investigated. The mean mass fractions of OH and C_2H_2 is shown in Fig. 9. The higher burning rate produces more hydroxyl for the variable diffusivity case, which will

increase the rate of soot oxidation shown in Fig. 10. Minor effect is found on acetylene, with slightly lower peak value for the variable diffusivity case, probably for higher consumption by the soot as will be shown later. The differences in the acetylene mass fraction is reflected on the soot nucleation rate shown in Fig. 11. However, Fig. 12 shows that the variable diffusivity case has higher soot surface growth rate. The higher surface growth rate indicates larger average soot particles surface area shown in Fig. 13 and higher soot number density (larger amount of particles) and soot average mass per unit volume (first moment) shown in Fig. 14. As discussed previously, the higher Lewis number for the constant diffusivity allows more heat to diffuse in the preheat zone, and that in turn, increases the collision frequency in the subgrid level, since the collision frequency is proportional to the temperature. As a result, more coagulation occur, which results in smaller number density, as shown in Fig. 14.

Figure 15 shows that the variable diffusion case predicts around double the peak value of the soot volume fraction of the other case. However, the constant diffusivity case shows a slightly wider profiles for the temperature and the soot volume fraction. The wider profile is a direct consequence of the higher Le (higher thermal diffusivity). The higher soot production is a direct result of the higher surface growth rate shown before in Fig. 12.

V. Conclusion

A LES subgrid model for soot formation has been developed by incorporating a method of moment approach within a subgrid mixing and combustion model. The coupled reaction-diffusion-MOMIC subgrid model requires no ad hoc filtering and allows exact estimate of the diffusion and kinetics processes within the small scales. A relatively detailed kinetics model is combined with a soot model and is used to study the effect of employing a detailed diffusion coefficients on the soot production in turbulent premixed flames. The results show that the variable diffusivity case shows a more symmetric curvature PDF with wider tails and more concave elements. The higher relative thermal to molecular diffusivity in the constant diffusion coefficients increases the collision frequency and the coagulation rate and that in turn reduces the number density and the soot surface growth rate.

Acknowledgements

At Georgia Tech, this work is supported by Army Research Office (Dr. David Mann), and at Princeton University, by the Air Force Office of Scientific Research (Dr. Julian Tishkoff) and the Air Force Research Laboratory (Dr. Skip Williams), respectively

References

[1]D'Alessio, A., D'Anna, A., Sgro, L. A., and Violi, A., "On the Relevance of Surface Growth in Soot Formation in Premixed Flames," *Proc. Combust. Inst.*, Vol. 20, 2000, pp. 2547–2554.

[2]Kim, C. H., El-Leathy, A. M., and Fath, G. M., "Soot Surface Growth and Oxidation in Laminar Diffusion Flames at Pressures of 0.1-1.0 atm," *Combust. and Flame*, Vol. 136, 2003, pp. 191–207.

[3]Frenklach, M. and Wang, H., "Detailed Modeling of Soot Particle Nucleation and Growth," *Proc. Combust. Inst.*, Vol. 23, 1990, pp. 1559–1566.

[4]Wang, H. and Frenklach, M., "Calculations of Rate Coefficients for Chemically Activated Reactions of Acetylene with Vinylic and Aromatic Radicals," *Journal of Phys. Chem.*, Vol. 98, 1994, pp. 11465–114893.

[5]Balthasar, M. and Mauss, M., "A Stochastic Approach to Calculate the Particle Size Distribution Function of Soot Particles in Laminar Premixed Flames," *Combust. and Flame*, Vol. 133, 2003, pp. 289 – 298.

[6]Colket, M. B. and Hall, R. J., *Success and Uncertainties in Modelling Soot Formation in Laminar, Premixed Flames*, Springer Verlag, Heidelberg, 1994.

[7]Young, K. J. and Moss, J. B., "Laminar Diffusion Flames Burning and Oxygen-Enriched Flames," *Combust. Sci. and Tech.*, Vol. 105, 1995, pp. 33–53.

[8]Balthasar, M. and Mauss, F., "Soot Formation in Turbulent Reacting Flows- A PDF-Based Approach Applied to Carbon Black Production," *Combust. and Flame*, Vol. 128, 2002, pp. 395 – 409.

[9]Erlebacher, G., Hussaini, M. Y., Speziale, C. G., and Zang, T. A., "Toward the Large-Eddy Simulation of Compressible Turbulent Flows," *Journal of Fluid Mechanics*, Vol. 238, 1992, pp. 155–185.

[10]Kim, W.-W., Menon, S., and Mongia, H. C., "Large-Eddy Simulation of a Gas Turbine Combustor Flow," *Combust. Sci. and Tech.*, Vol. 143, 1999, pp. 25–62.

[11]Kim, W.-W. and Menon, S., "Numerical Simulations of Turbulent Premixed Flames in the Thin-Reaction-Zones Regime," *Combust. Sci. and Tech.*, Vol. 160, 2000, pp. 119–150.

[12]Menon, S. and Calhoon, W., "Subgrid Mixing and Molecular Transport Modeling for Large-Eddy Simulations of Turbulent Reacting Flows," *Proc. Combust. Inst.*, Vol. 26, 1996, pp. 59–66.

[13]Menon, S., Yeung, P.-K., and Kim, W.-W., "Effect of Subgrid Models on the Computed Interscale Energy Transfer in Isotropic Turbulence," *Computers and Fluids*, Vol. 25, No. 2, 1996, pp. 165–180.

[14]Kim, W.-W. and Menon, S., "A New Incompressible Solver for Large-Eddy Simulations," *International Journal of Numerical Fluid Mechanics*, Vol. 31, 1999, pp. 983–1017.

[15]Sankaran, V. and Menon, S., "Alignment Statistics and Small-Scale Structures in Swirling Spray Combustion," *Proc. Combust. Inst.*, Vol. 29, 2002, pp. 577–584.

[16]Eggenspieler, G. and Menon, S., "Combustion and Emission Modelling near Lean Blow-Out in a Gas Turbine Engine," *Progress in Computational Fluid Dynamics*, Vol. 5, No. 6, 2005, pp. 281–297.

[17]Fureby, C. and Möller, S.-I., "Large-Eddy Simulation of Reacting Flows Applied to Bluff Body Stabilized Flames," *AIAA Journal*, Vol. 33, No. 12, 1995, pp. 2339–2347.

[18]Chakravarthy, V. K. and Menon, S., "Large-Eddy Simulations of Turbulent Premixed Flames in the Flamelet Regime," *Combust. Sci. and Tech.*, Vol. 162, 2000, pp. 175–222.

[19]Sankaran, V. and Menon, S., "LES of Scalar Mixing in Supersonic Shear Layers," *Proc. Combust. Inst.*, Vol. 30, No. 2, 2005, pp. 2835–2842.

[20]Chakravarthy, V. K. and Menon, S., "Linear-Eddy Simulations of Reynolds and Schmidt Number Dependencies in Turbulent Scalar Mixing," *Phys. of Fluids*, Vol. 13, 2001, pp. 488–499.

[21]Sankaran, V. and Menon, S., "Subgrid Combustion Modeling of 3-D Premixed Flames in the Thin-Reaction-Zone Regime," *Proc. Combust. Inst.*, Vol. 30, No. 1, 2005, pp. 575–582.

[22]El-Asrag, H. and Menon, S., "Large Eddy Simulation of Swirling Non- Premixed Flame," *AIAA-2005-3971*, 2005.

[23]Menon, S., "CO Emission and Combustion Dynamics Near Lean Blow-Out in Gas Turbine Engines," *ASME-GT2004-53290*, 2004.

[24]Menon, S. and Patel, N., "Subgrid Modeling for LES of Spray Combustion in Large-Scale Combustors," *AIAA Journal (to appear, 2006)*, 2006, pp. In Press.

[25]Harris, S. J. and Weiner, A. M., "Some Constraints on Soot Particle Inception in Premixed Ethylene Flames," *Proc. Combust. Inst.*, Vol. 20, 1984, pp. 969–978.

[26]Xu, F., Sunderland, P. B., and Faeth, G. M., "Soot formation in Laminar Premixed Ethylene/Air Flames at Atmospheric Pressure," *Combust. and Flame*, Vol. 108, 1997, pp. 471 – 493.

[27]Lindstedt, P. R., *Soot Formation in Combustion*, Springer Verlag, Heidelberg, 1994.

[28]Lu, T. and Law, C. K., "A Directed Relation Graph Method for Mechanism Reduction," *Proc. Combust. Inst.*, Vol. 30, 2005, pp. 1333 – 1341.

[29]Law, C. K., "Private Communication," .

[30]Qin, Z., Lissianski, V. V., Gardiner, W. C., Davis, S. G., and Wang, H., "A Directed Relation Graph Method for Mechanism Reduction," *Proc. Combust. Inst.*, Vol. 28, 2000, pp. 1663 – 1669.

[31]Lu, T. and Law, C. K., "Complex CSP for Chemistry Reduction and Analysis," *Combust. and Flame*, Vol. 126, 2001, pp. 1445–1455.

[32]Lee, K. B., Thring, M. W., and Beer, J. M., "On the Rate of Combustion of Soot in a Laminar Soot Flame," *Combust. and Flame*, Vol. 6, 1962, pp. 137 – 145.

[33]Bradley, D., Dixon-Lewis, G., El-Din Habik, S., and Mushi, E. M. J., "The Oxidation of Graphite Powder in Flame Reaction Zones," *Proc. Combust. Inst.*, Vol. 20, 1984, pp. 931 – 940.

[34]Frenklach, M., "Method of Moments with interpolative closure," *Chem. Eng. Sci.*, 2002, pp. 2229–2239.

[35]Friedlander, S. K., *Smoke, Dust, and Haze Fundamentals of Aerosol Dynamics*, Oxford University Press, 2000.

[36]Kerstein, A. R., "Linear-Eddy Model of Turbulent Transport II," *Combust. and Flame*, Vol. 75, 1989, pp. 397–413.

[37]Harris, S. J. and Weiner, A. M., "Chemical Kinetics of Soot Particle Growth," *Ann. Rev. of Phys. Chem.*, 1985, pp. 31–52.

[38]Smoluchowski, M. V., *Z. Phys. Chem.*, Vol. 92, 1917, pp. 129–139.

[39]Zhigang, L. and Wang, H., "Drag Force, diffusion coefficient and electric mobility of small particles. I. Theory applicable to a free-molecule regime," *Phys. Review E*, Vol. 68, 2003, pp. 061206–1–061206–9.

[40]Seinfeld, J. H. and Pandis, S. N., *Atmosperic Chemistry and Physics. From Air Pollution to Climate Change*, New York: Willy, 1998.

[41]Kazakov, A. and Frenklach, M., "Dynamic Modeling of Soot Particle Coagulation and Aggregation:Implementation with the Method of Moments and Application to High-Pressure Laminar Premixed Flames," *Combust. and Flame*, Vol. 114, 1998, pp. 484–501.

[42]Stephen, J. and Kennedy, I. M., "Soot Particle Aerosol Dynamics at High Pressure," *Combust. and Flame*, Vol. 78, 1989, pp. 390–397.

[43]Pratsinis, S. E., "Simultaneous nucleation, condensation, and coagulation in aerosol reactors," *Journal of Collide and Interface Science*, Vol. 124, 1988, pp. 416–427.

[44]Wagner, H. G., "Soot Formation in Combustion," *Proc. Combust. Inst.*, Vol. 17, 1979, pp. 3–19.

[45]Gordon, L. D., "Effect of Initial Temperature on Flame Speed of Methane-Air, Propane-Air, and Ethylene-Air mixtures," *NACA TN 2170, Report 1061*, 1950, pp. 105–116.

[46]Lima, J. A., Marin, E., and S., S. M., "Characterization of the thermal properties of gases using a thermal wave interferometer," *Meas. Sci. Technol.*, 2001, pp. 1949 – 1955.

[47]Trouvé, A. and Poinsot, T., "The Evolution Equation for the Flame Surface Density in Turbulent Premixed Combustion," *Journal of Fluid Mech.*, Vol. 278, 1994, pp. 1–31.

[48]Pope, S. B., "Computationally Efficient Implementation of Combustion Chemistry Using In Situ Adaptive Tabulation," *Combust. Theory Modelling*, Vol. 1, 1997, pp. 41–63.

[49]Law, C. K., Cho, P., Mizomoto, M., and Yoshida, H., "Flame Curvature and Preferential Diffusion in the Burning Intensity of Bunsen Flames," *Proc. Combust. Inst.*, Vol. 21, 1986, pp. 1803–1809.

[50]Mizomoto, M., Asaka, Y., Ikai, S., and Law, C. K., "Effects of Preferential Diffusion on the on the Burning Intensity of Curved Flames," *Proc. Combust. Inst.*, Vol. 20, 1984, pp. 1933–1939.

[51]Echekki, T. and Chen, J. H., "Unsteady Strain Rate and Curvature Effects in Turbulent Premixed Methane-Air Flames," *Combust. and Flame*, Vol. 106, No. 1, 1996, pp. 184–202.

[52]Bradley, D., Gaskell, P. H., Sedaghat, X. J., and Gu, X. J., "Generation of PDFS for Flame Curvature and for Flame Stretch Rate in Premixed Turbulent Combustion," *Combust. and Flame*, Vol. 135, 2003, pp. 503 – 523.

[53]Pocheau, A., "Scale Invariance in Turbulent Front Propagation," *Phys. Rev. E*, Vol. 49, 1994, pp. 1109–1122.

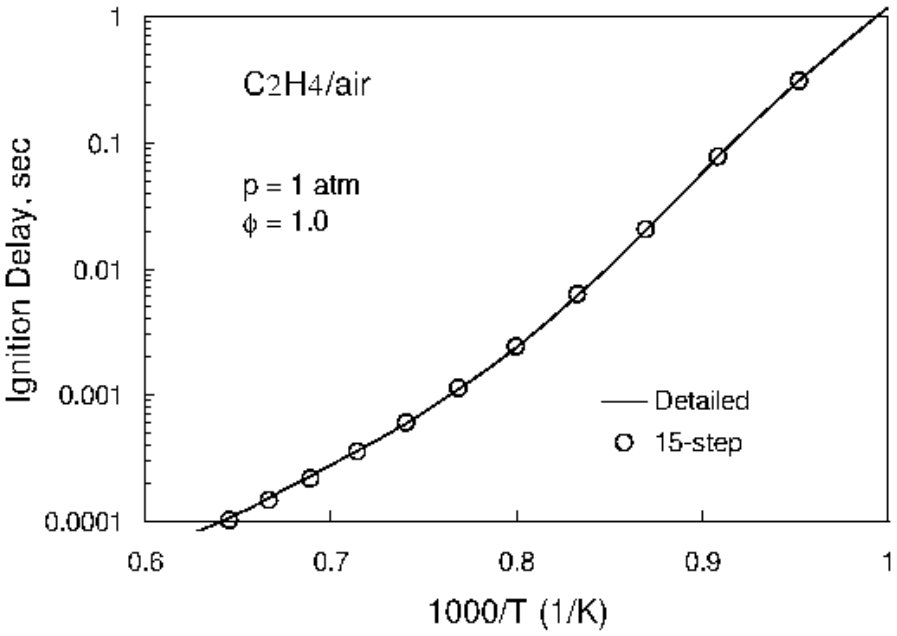

Figure 1. Comparison of ignition delay

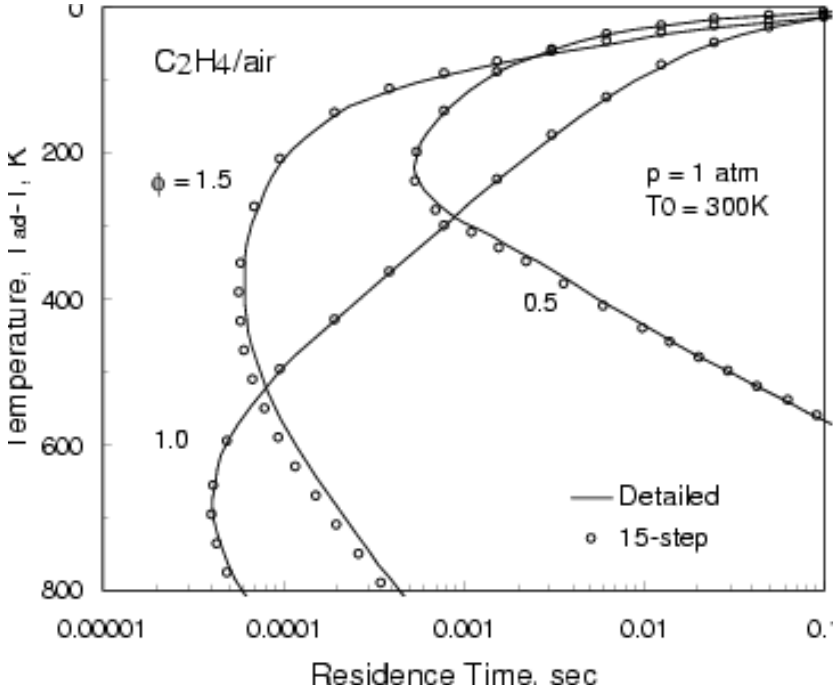

Figure 2. Comparison of temperature profiles

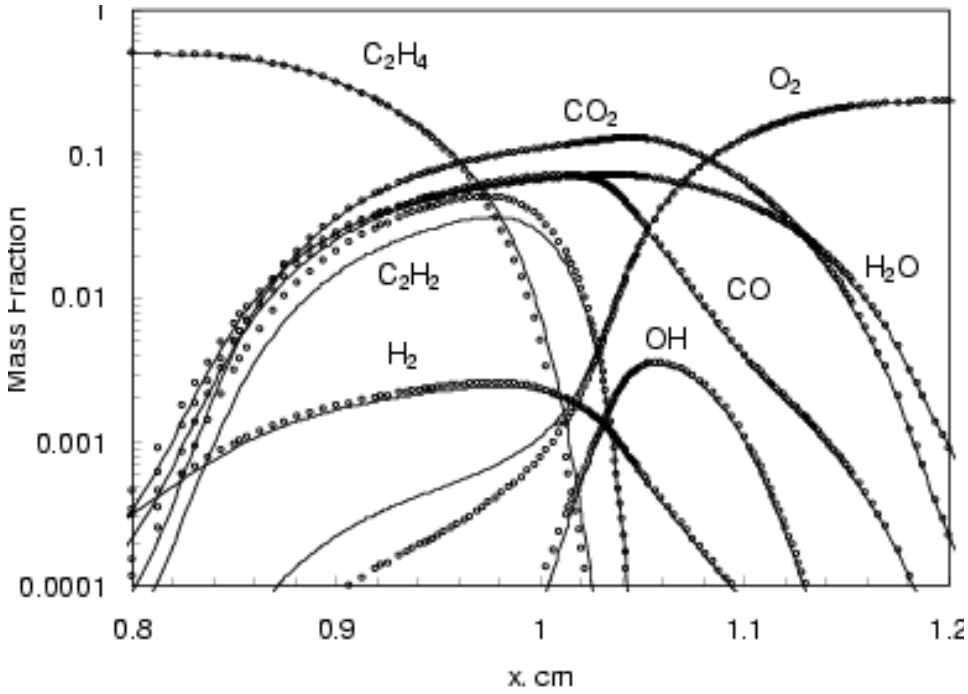

Figure 3. Comparison of species profiles of counterflow diffusion flame

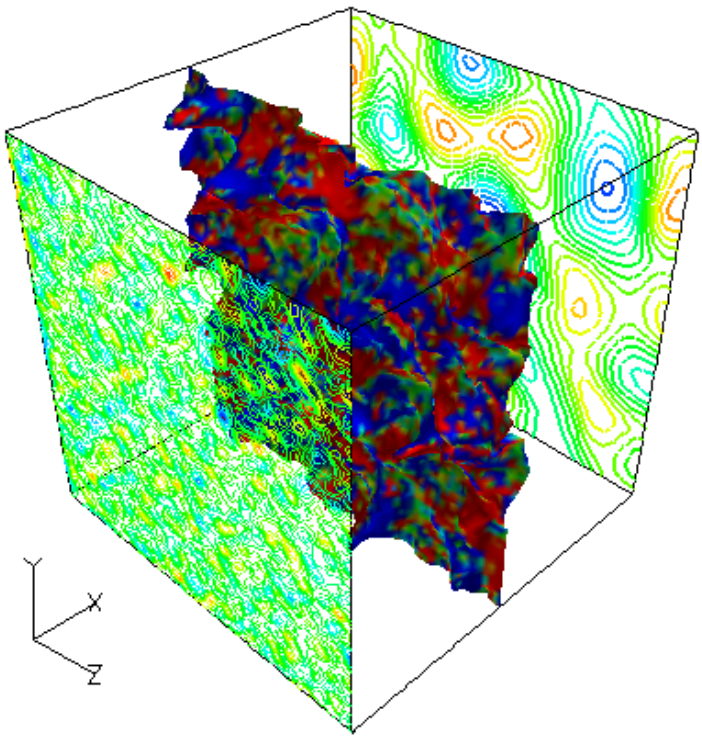

Figure 4. Temperature iso-surface (T = 1600 K) with inflow outflow vorticity contours

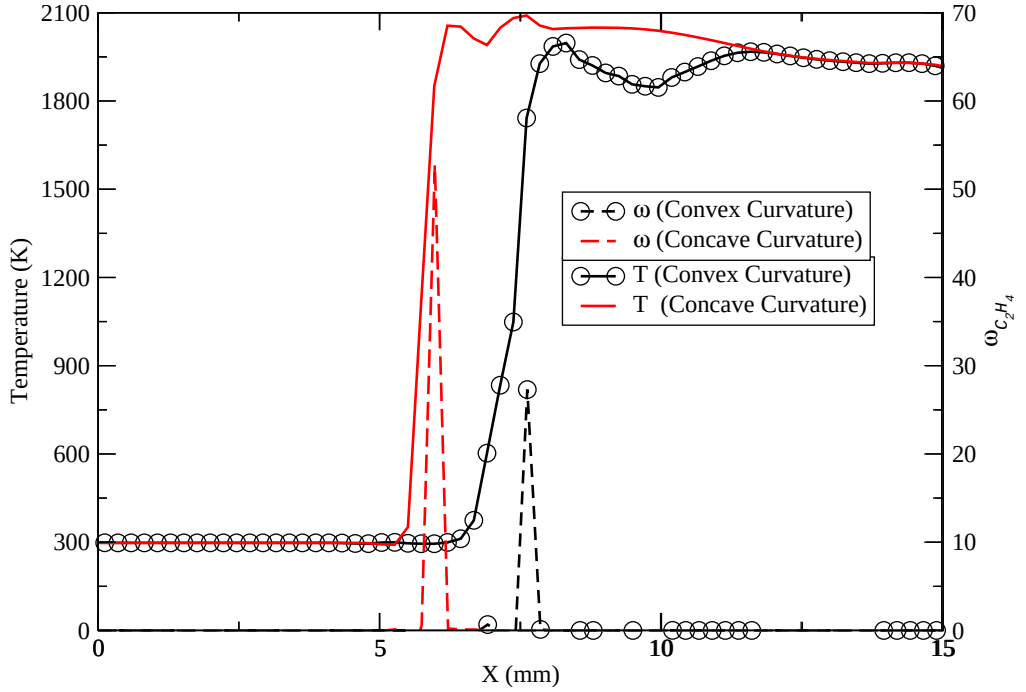

Figure 5. Instantaneous temperature and C_2H_4 reaction rate at a convex and concave flame segments with variable diffusion coefficients

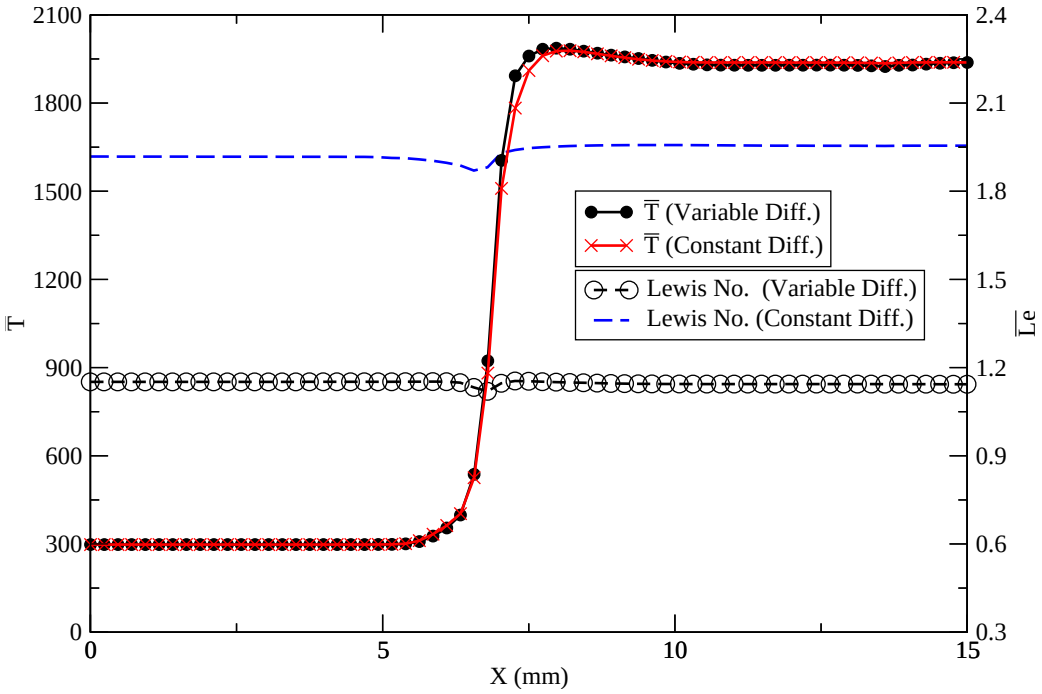

Figure 6. Mixture mean Lewis number and mean temperature profile comparison

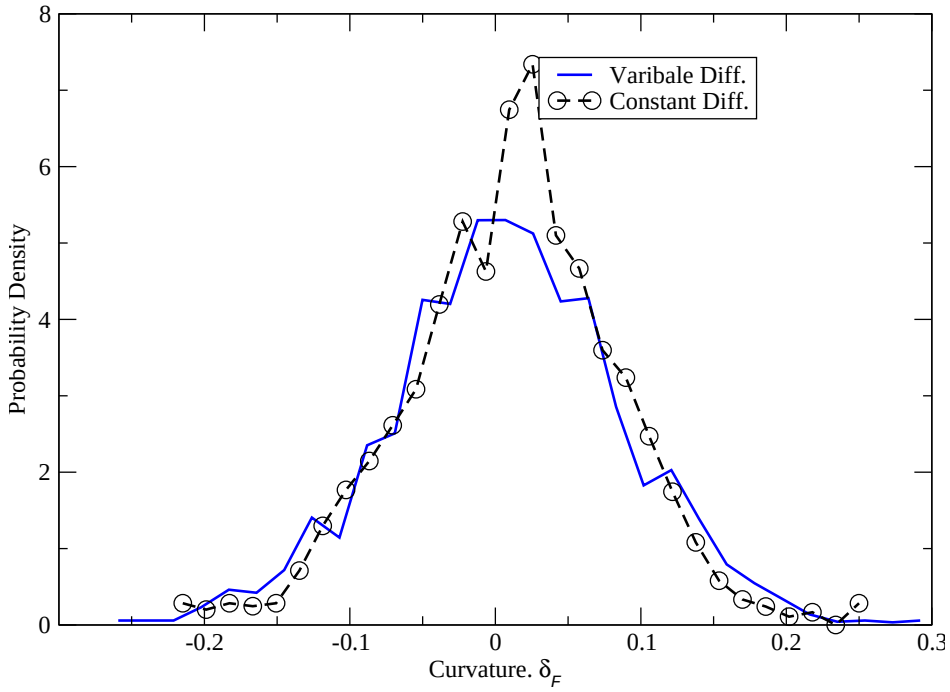

Figure 7. Mean Curvature probability density function (PDF)

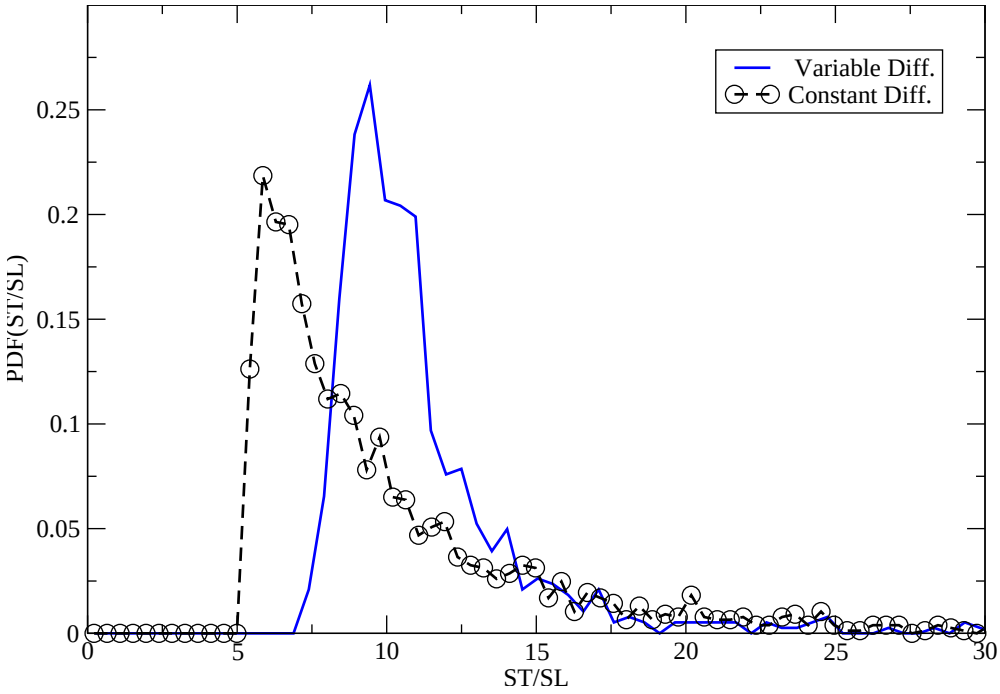

Figure 8. Mean normalized turbulent flame speed probability density function (PDF)

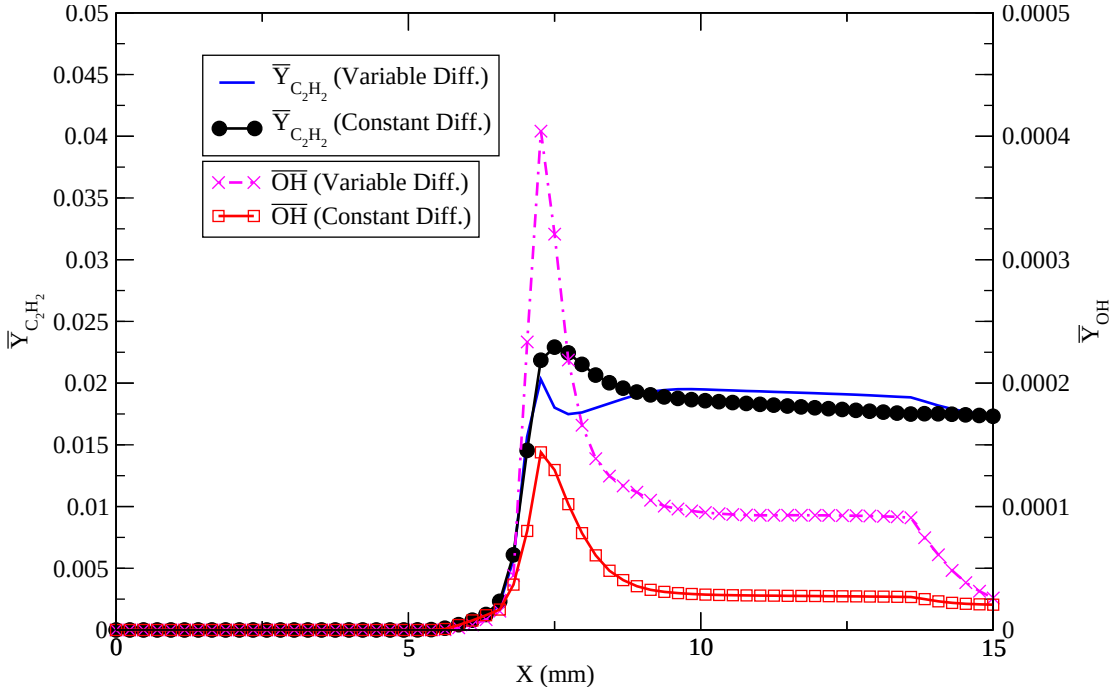

Figure 9. Mean mass fraction of acetylene C_2H_2 and hydroxyl OH

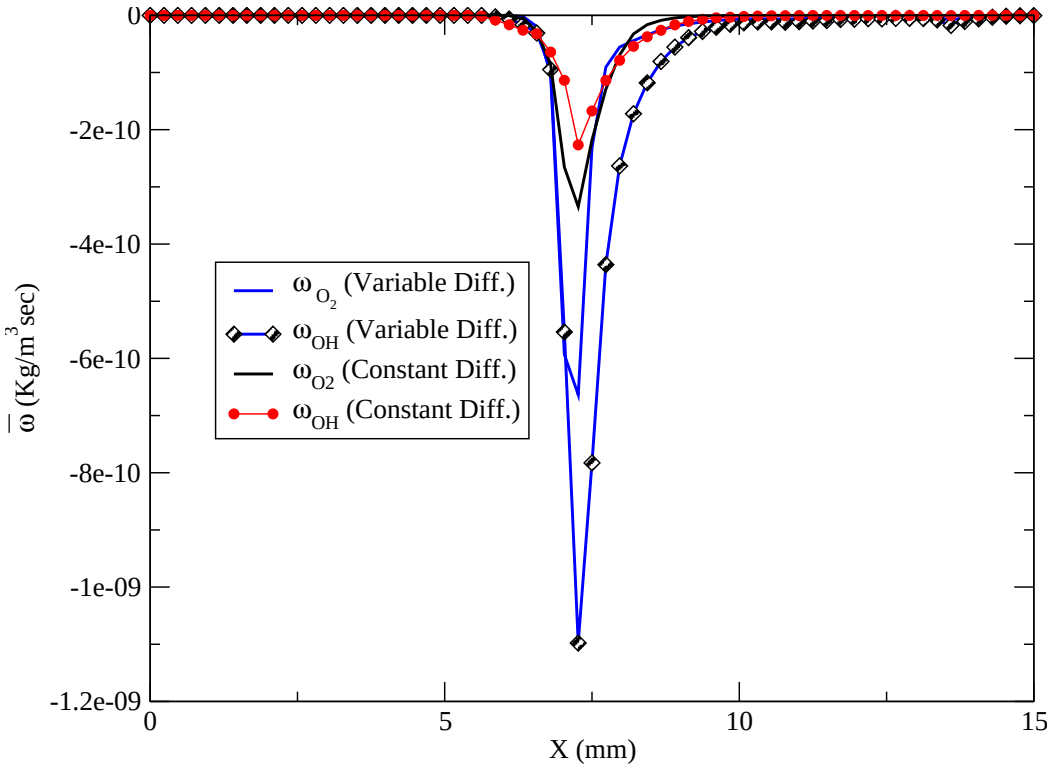

Figure 10. Soot oxidation rates

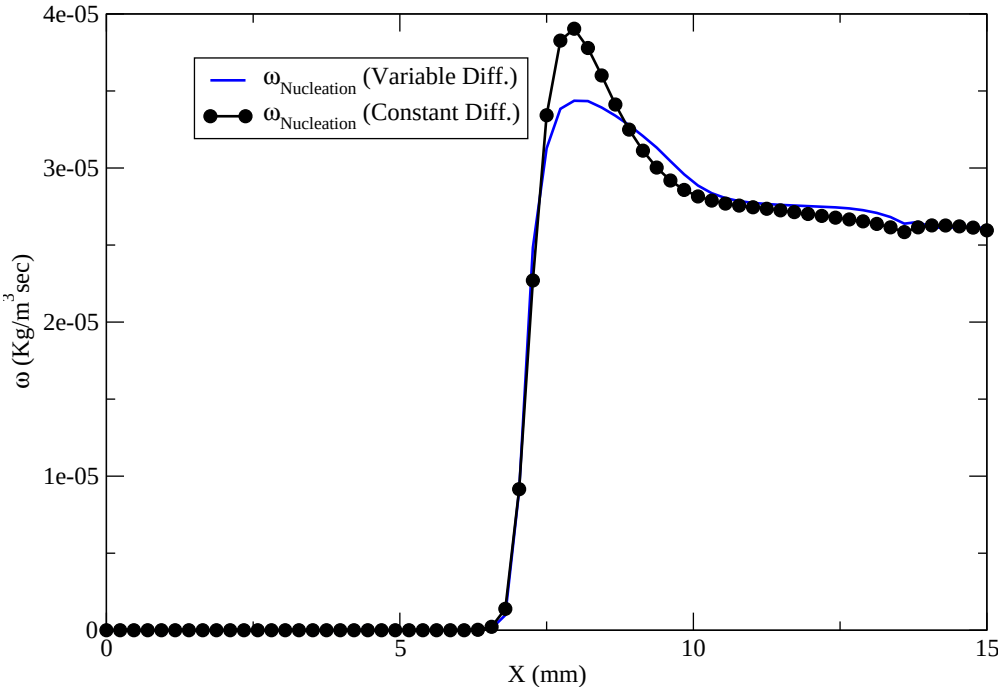

Figure 11. Soot nucleation rate

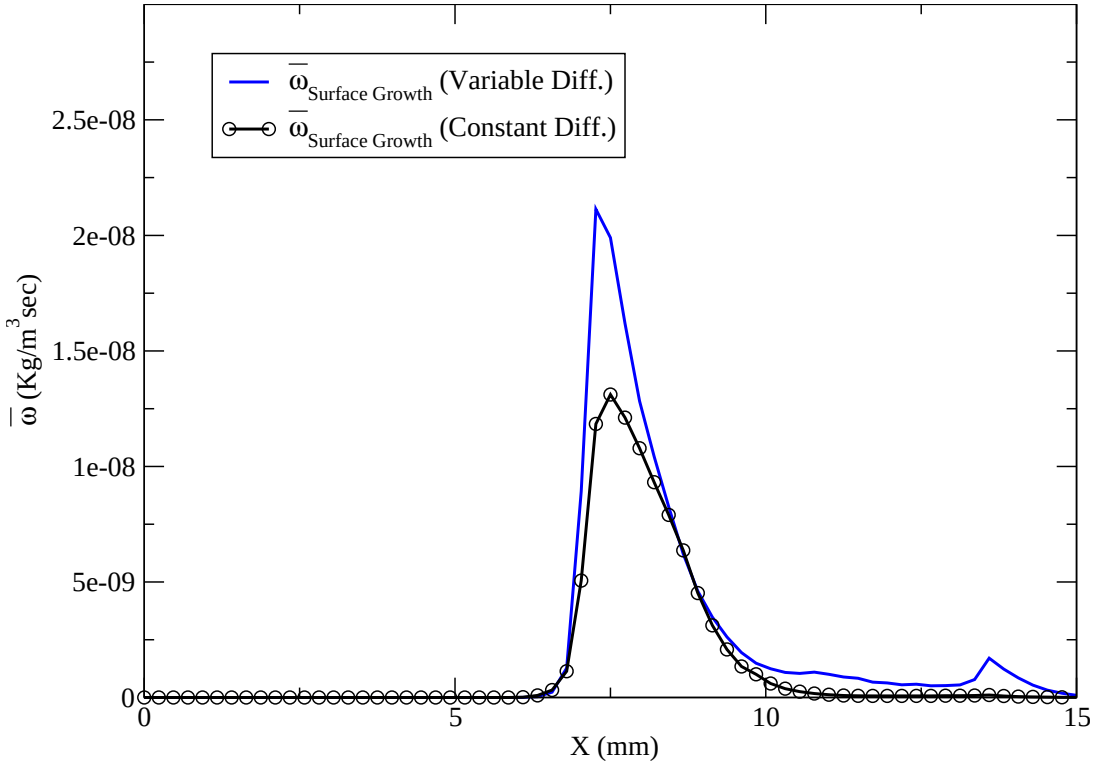

Figure 12. Soot surface growth

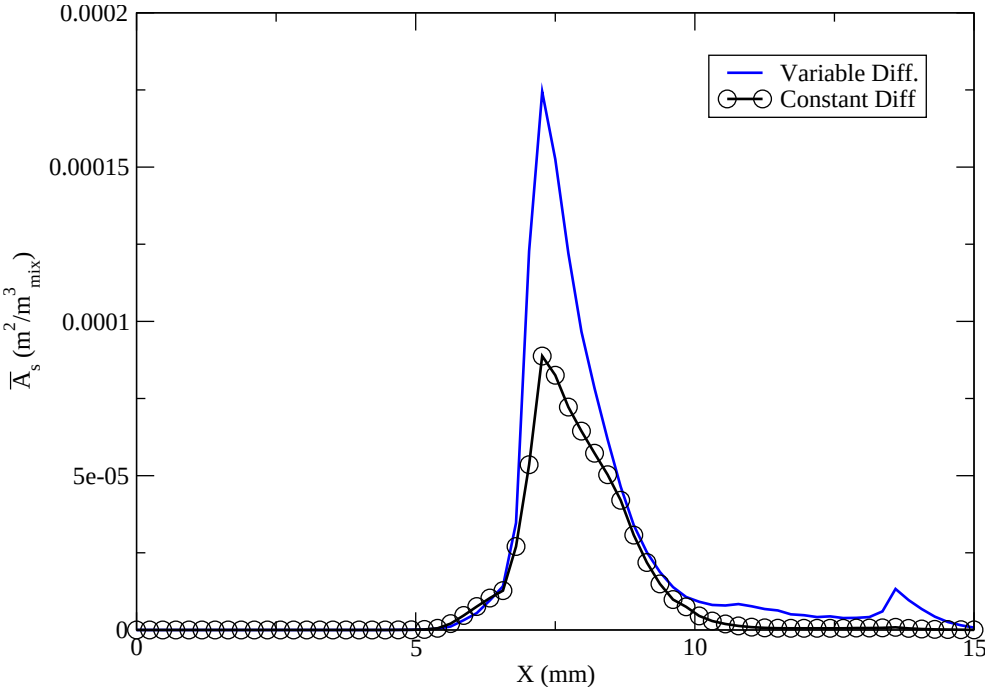

Figure 13. Mean soot surface area per unit mixture volume

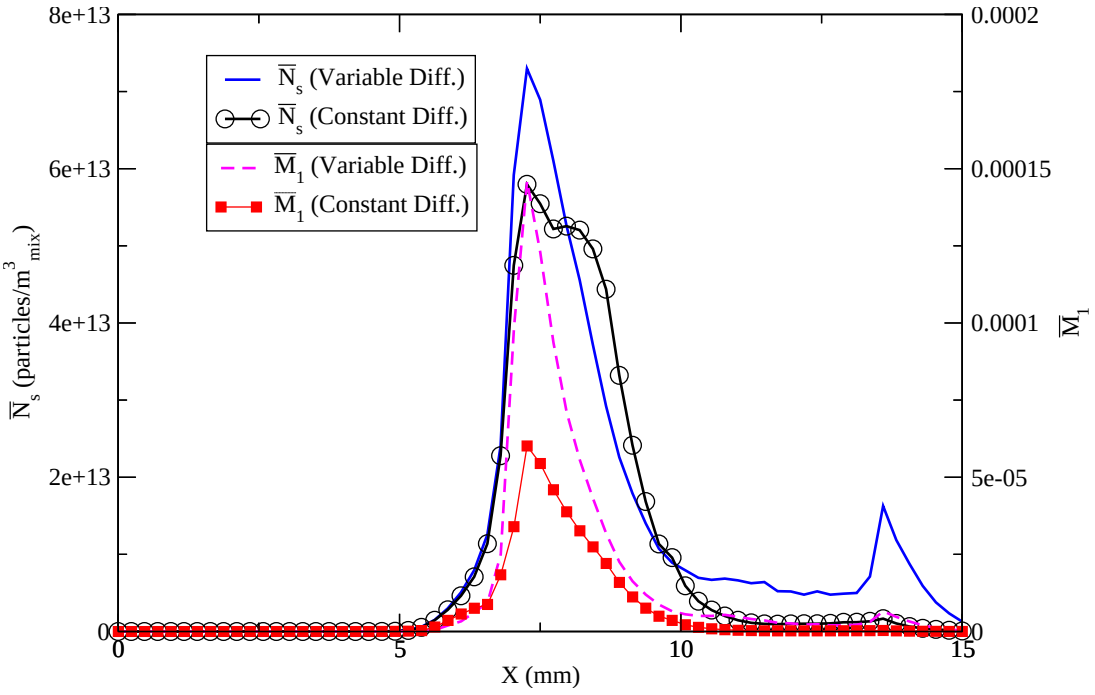

Figure 14. Mean soot surface area per unit mixture volume

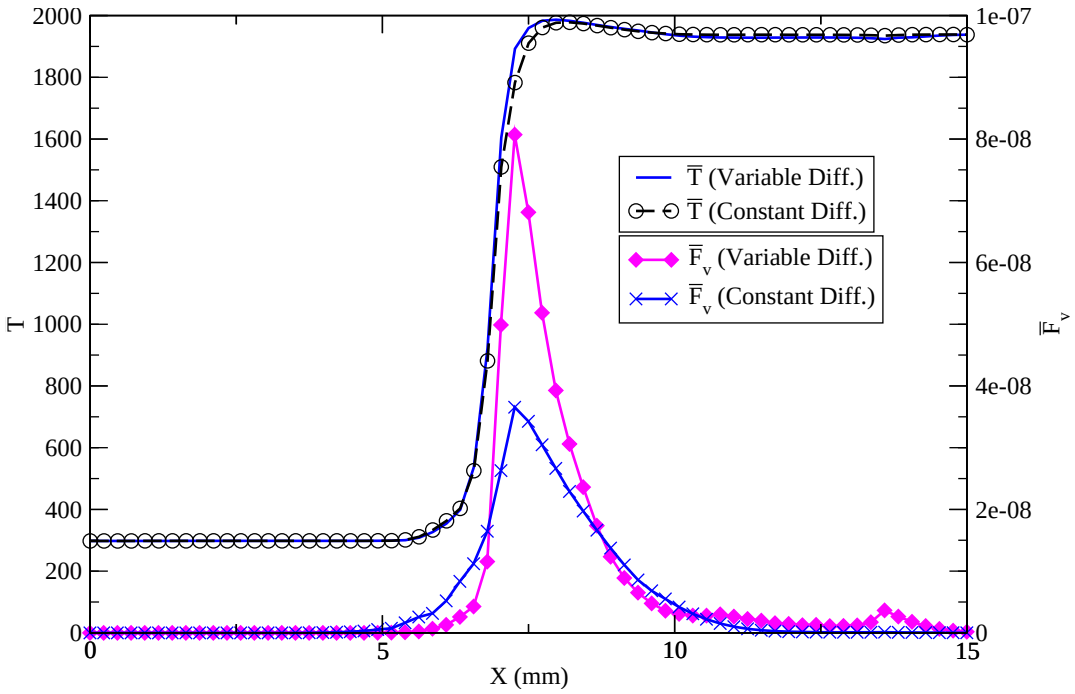

Figure 15. Mean soot volume fraction and temperature profile